



DOI: 10.18720/MCE.94.11

## Finite element modeling of cold-formed steel deck in bending

V.V. Degtyarev\*

New Millennium Building Systems, LLC, Columbia, SC, USA

\* E-mail: [vitaliy.degtyarev@newmill.com](mailto:vitaliy.degtyarev@newmill.com)

**Keywords:** cold-formed steel deck, flexural behavior, buckling, bending strength, finite element method, numerical methods, ANSYS

**Abstract.** Finite element simulations of structural members are a good alternative to physical testing for studying strength and structural response of the members when finite element models have been properly calibrated and validated. Published information on finite element modeling of cold-formed steel deck in bending is scarce. This paper presents the development of finite element models of corrugated steel deck in bending using a general-purpose software, ANSYS. Effects of the following parameters on elastic buckling and ultimate moments of models, as well as on their load-deflection curves, were studied: shell element types, mesh density, corner radius, number of deck corrugations, presence of transverse ties, initial geometric imperfection distribution and magnitude, deck boundary conditions, loading type, and stress-strain diagrams. Optimal parameters of the models were determined. Moment capacities, flexural stiffness, and load-deflection curves predicted by the models with the optimal parameters correlated well with test results available in literature, especially when the deck material behavior was described by nonlinear stress-strain diagrams. The developed FE models can be used for studying flexural strength and behavior of solid steel deck with various geometry under various loading types, which can be useful in development of new efficient profiles and in improving the current deck design methods. The models can also be used as a basis for the development of FE models of steel deck with openings and acoustical perforations, as well as built-up deck profiles, design methods for which are currently underdeveloped.

### 1. Introduction

Corrugated cold-formed steel (CFS) deck, which is available in many different shapes and depths, has been widely used in construction throughout the world. Figure 1 shows two representatives of the deck manufactured and used in Europe. Structural design of corrugated steel deck in different countries is governed by national standards [1–4]. Some countries also have manuals [5, 6], which offer additional guidance on the design and construction with steel decks. Despite the wide use of corrugated steel decks, some items, such as design of perforated steel deck [7, 8], deck with openings [5, 9], deck under concentrated loads [1, 6, 10, 11], and built-up deck sections, are not covered at all or covered with significant limitations in the design standards and manuals. Questions about the accuracy of flexural strength prediction of some deck profiles by the direct strength method adopted in [1] have been recently raised [12, 13]. There is an obvious need for additional research of strength and structural behavior of certain types of corrugated steel deck and steel deck under certain types of loads.

Physical testing has been traditionally considered as the most reliable way of obtaining information about the performance of structural members and systems. Physical testing, however, requires significant resources, which makes its use problematic for extensive studies, which involve wide ranges of design parameters. Finite element (FE) method, on the other hand, is an efficient alternative to physical testing when FE models have been properly validated and calibrated against available test data [14]. It allows for performing extensive parametric studies using limited resources. FE simulations can also give detailed information about elastic buckling loads of the deck and stress/strain distributions in deck profiles, obtaining of which from physical testing can be difficult.

Many researchers have successfully used FE method for simulations of CFS structural members under various loading types resulting in different failure modes [15–29]. FE models of CFS structural members were created using shell elements in different commercially available FE programs. It has been shown that the FE

Degtyarev, V.V., Finite element modeling of cold-formed steel deck in bending. Magazine of Civil Engineering. 2020. 94(2). Pp. 129–144. DOI: 10.18720/MCE.94.11



This work is licensed under a CC BY-NC 4.0

method can capture specifics of structural behavior of CFS structural members. It should be noted, however, that the majority of FE models of CFS structural members have been developed for C- and Z-shaped sections. There is a limited number of published papers on FE modeling of CFS deck in bending [10, 11, 30]. The available papers dealt with some specific applications, such as steel deck under concentrated loads and perforated deck, and do not discuss general FE modeling of CFS steel deck in bending.

The objectives of this paper are to develop FE models of corrugated CFS deck in bending, validate them using available test data, and study the effects of different parameters of the models on their elastic buckling moments, moment capacity, and structural response. The FE models were developed in a commercial general-purpose software, ANSYS [31] and validated against physical test data published in [32]. Effects of the following FE model parameters on their elastic buckling, ultimate strength, and structural response were studied: shell element type, mesh density, corner radius, number of deck corrugations, presence of transverse ties, initial geometric imperfection (IGI) distribution and magnitude, deck boundary conditions, loading type, and the material model of steel. Optimal parameters of the FE models for simulating steel deck strength and behavior in bending were determined from the study. The developed FE models can be used for studying flexural strength and behavior of solid steel deck with various geometry and loading types. The models can also be used as a basis for development of FE models of steel deck with acoustical perforations and openings, as well as built-up deck profiles.

## 2. Methods

FE models of CFS deck profiles shown in Figure 1 were developed in a commercial general-purpose software, ANSYS [31], using structural shell elements. The profiles were physically tested at the Karlsruhe Institute of Technology (KIT) for the research project titled "Guidelines and Recommendations for Integrating Specific Profiled Steel Sheets in the Eurocodes (GRISPE)" [32]. In the project, deck types JI\_73-195-780 and JI\_56-225-900 shown in Figure 1 with the nominal steel thickness of 0.75 and 1.00 mm were tested in bending in accordance with EN 1993-1-3:2006 [4]. The deck was produced by Joris Ide from galvanized steel grade S320GD according to EN 10346:2009 [33] with the nominal yield strength of 320 MPa. Results of 14 physical tests of solid deck in bending published in [32] were used for development and validation of FE deck models described in this paper.

Single deck sheets shown in Figure 1 installed in single 3300-mm long spans were tested in six-point bending simulating a uniformly distributed load. The deck was supported at top flanges with timber blocks to prevent web crippling. Timber blocks were also used to transfer loads to the deck bottom flanges. Transverse ties were provided at the load locations and near supports to prevent deck sheets from spreading. The failure loads and load-deflection curves were obtained from the tests for every tested specimen and presented in [32]. The mechanical properties of the steel used for fabrication of the tested deck specimens were determined from tensile tests of steel coupons. The base steel thickness, excluding zinc coating, was also determined.

In the FE models, the actual base steel thickness and mechanical properties of the deck reported in [32] were used. The study consisted of seven stages. In each stage, effects of one or several of the following parameters on the elastic buckling moments, moment capacity, and structural response of steel deck models were evaluated: shell element type, mesh density, corner radius, number of deck corrugations, presence of transverse ties, IGI distribution and magnitude, deck boundary conditions, loading type and stress-strain diagrams of steel. The following sections describe FE models used in each stage and discuss obtained results.

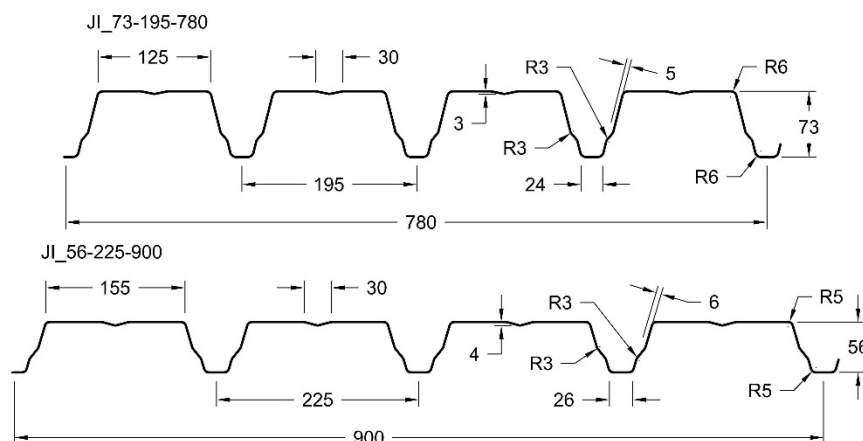


Figure 1. Dimensions [mm] of the deck profiles used for the development of FE models.

### 3. Results and Discussion

#### 3.1. Effects of element type, mesh density, and initial geometric imperfection magnitude

In this stage, the effects of mesh density and element type on elastic buckling and ultimate moments were studied on the 73-mm deep deck with the nominal steel thickness of 0.75 mm and on the 56-mm deep deck with the nominal steel thickness of 1.00 mm. The selected deck profiles represented the lower and upper bounds of the deck heights and thicknesses considered in the study. Effects of IGI magnitude on the deck moment capacity were also evaluated.

Four-node and eight-node structural shell elements, SHELL181 and SHELL281, respectively, with five integration points were used for modeling the deck. Both element types have six degrees of freedom at each node. They are well suited for large-strain nonlinear applications and are capable of accounting for shell thickness change in nonlinear analyses. SHELL181 is a linear shell element. SHELL281 is a quadratic shell element. Quadratic shell elements generally allow for the use of coarser meshes, give greater flexibility in FE model meshing, and result in improved convergence of the solution when compared with linear shell elements [14]. The use of quadratic elements, however, results in considerably longer computation times.

Multilinear isotropic hardening models (MISO) with von Mises plasticity were used to define the material behavior of steel deck. The deck stress-strain curves were described by the nonlinear models proposed in [34] (Figure 2). The key input parameters of the models were determined using the yield stress and tensile strength of the steel obtained from coupon tests in [32]. An elastic modulus of  $2.03 \times 10^5$  MPa and a Poisson's ratio of 0.3 were used. The engineering stresses and strains were converted into the true stresses and strains using the following well-known relationships from Appendix C.6 of EN 1993-1-5:2006 [35]:  $f_{true} = f_{eng}(1 + \epsilon_{eng})$ , where  $f_{true}$  and  $f_{eng}$  are true and engineering stresses, respectively, and  $\epsilon_{true} = \ln(\epsilon_{eng} + 1)$ , where  $\epsilon_{true}$  and  $\epsilon_{eng}$  are true and engineering strains, respectively.

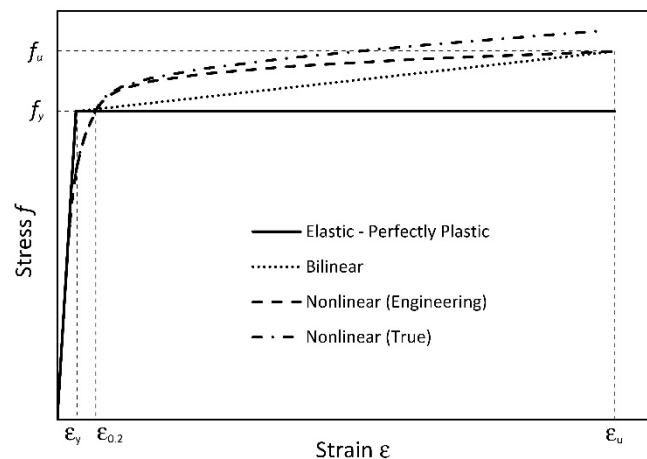


Figure 2. Steel stress-strain diagrams.

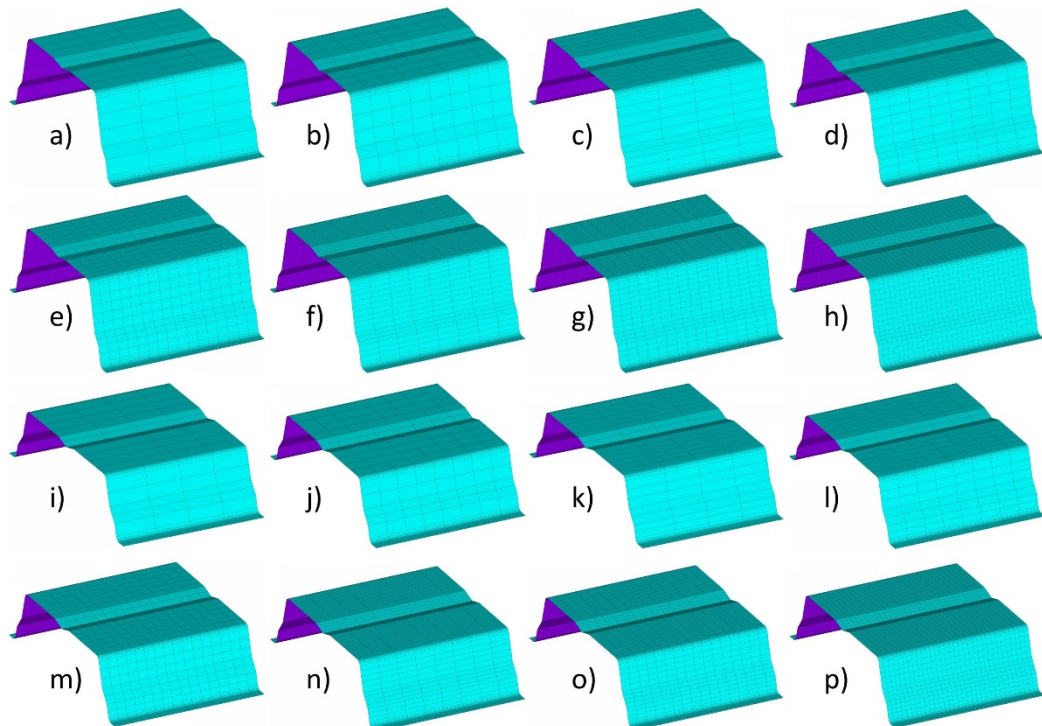
The deck models were meshed with quadrilateral elements. To determine an optimal mesh density, eight different mesh sizes shown in Table 1 and Figure 3 were considered. Corner radii of  $6+t/2$  and  $5+t/2$  mm (where  $t$  is the measured base steel thickness) were included for the models of the 73- and 56-mm deep decks, respectively, at the intersections of the deck top and bottom flanges with the deck webs. The web and top flange longitudinal stiffeners were modeled with sharp corners due to the small actual inside corner radii and large angles between the elements.

Table 1. Parameters of FE meshes considered in convergence study.

Mesh density designation	Maximum element size (mm) in the direction		Total number of elements	
	Perpendicular to deck length	Parallel to deck length	73-mm deck	56-mm deck
D1	15	40	6992	6624
D2	15	20	13528	14240
D3	10	40	9200	8096
D4	10	20	17800	17088
D5	10	10	35400	33984
D6	5	20	27056	27056
D7	5	10	53808	53808
D8	5	5	106704	106704

Figure 4 shows boundary conditions of deck models supported at top flanges and loaded through bottom flanges, which are referred to as TFS-BFL (top-flange-supported-bottom-flange-loaded) models hereafter. The symmetry in boundary and loading conditions allowed to model one-half of the deck span with the ANSYS symmetry degree-of-freedom constraints applied to the FE model nodes at the deck mid-span. At the deck support, vertical translations of nodes at the deck top flanges were restrained. To prevent rigid body motion, lateral displacement of one node at the edge of the deck bottom flange was restrained. The loads were modeled by forces applied to the deck bottom flanges. The forces applied at the deck longitudinal edges were two times smaller than the forces applied to the internal bottom flanges due to the smaller tributary widths of the edge bottom flanges. The nodes of each bottom flange at the load locations were coupled independently from the adjacent bottom flanges. The transverse ties used in the tests were modeled by coupling lateral displacements of the nodes at the deck panel edges at the load locations and near the deck supports.

Each model was analyzed in two steps: 1) elastic buckling analysis was performed to obtain elastic buckling modes and moments; 2) non-linear static analysis was performed with the IGI distribution based on the first elastic buckling mode obtained from the elastic buckling analysis. The first elastic buckling mode of both studied deck profiles was distortional buckling of the deck top flange characterized by vertical deformations of the top flange longitudinal stiffener (Figure 5a). The deck models also demonstrated local buckling of the top flange between the web and the longitudinal stiffener as one of the higher buckling modes (Figure 5b). Three different IGI magnitudes of  $0.15t$ ,  $0.64t$ , and  $b_{tf}/150$ , where  $b_{tf}$  is the deck top flange width, recommended in [36, 37, 23] were used in the models to study the effect of the IGI magnitude on the moment capacity. The absolute IGI magnitude values based on the measured deck dimensions were 0.10, 0.45, and 0.83 mm for the 73-mm deep deck with the nominal thickness of 0.75 mm and 0.14, 0.59, and 1.03 mm for the 56-mm deep deck with the nominal thickness of 1.00 mm. Large-deflection effects were included into the FE models to account for the geometric nonlinearity.



**Figure 3. Mesh densities used in convergence study (one 160 mm long deck flute is shown for clarity): a) to h) 73-mm deep deck with mesh densities D1 to D8, respectively; i) to p) 56-mm deep deck with mesh densities D1 to D8, respectively.**

Figure 6 shows the effects of the mesh density on the elastic buckling moments of the studied profiles. The distortional elastic buckling moments,  $M_{crd}$ , were practically independent of the mesh density for all studied models. On the other hand, the local elastic buckling moments,  $M_{crl}$ , were sensitive to the element sizes for the coarser meshes. For the coarser meshes, the numbers of top flange elements between the deck web and the stiffener were 3 and 4 for the 73- and 56-mm deep profiles, respectively (see Figure 3). These limited numbers of elements were insufficient for an accurate capturing of the local elastic buckling moments, especially for the linear 4-node elements. The local elastic buckling moments of the 73-mm deck models with the 4- and 8-node elements converged for the mesh densities D7 and D5, respectively. The local elastic buckling moments of the 56-mm deck models with the 4- and 8-node elements converged for the mesh densities D5 and D4, respectively. For these meshes, the number of top flange elements between the deck web and the stiffener were 9 and 5 for the 73-mm deck models with the 4- and 8-node elements, respectively, and 6 for the 56-mm deck models with both element types.

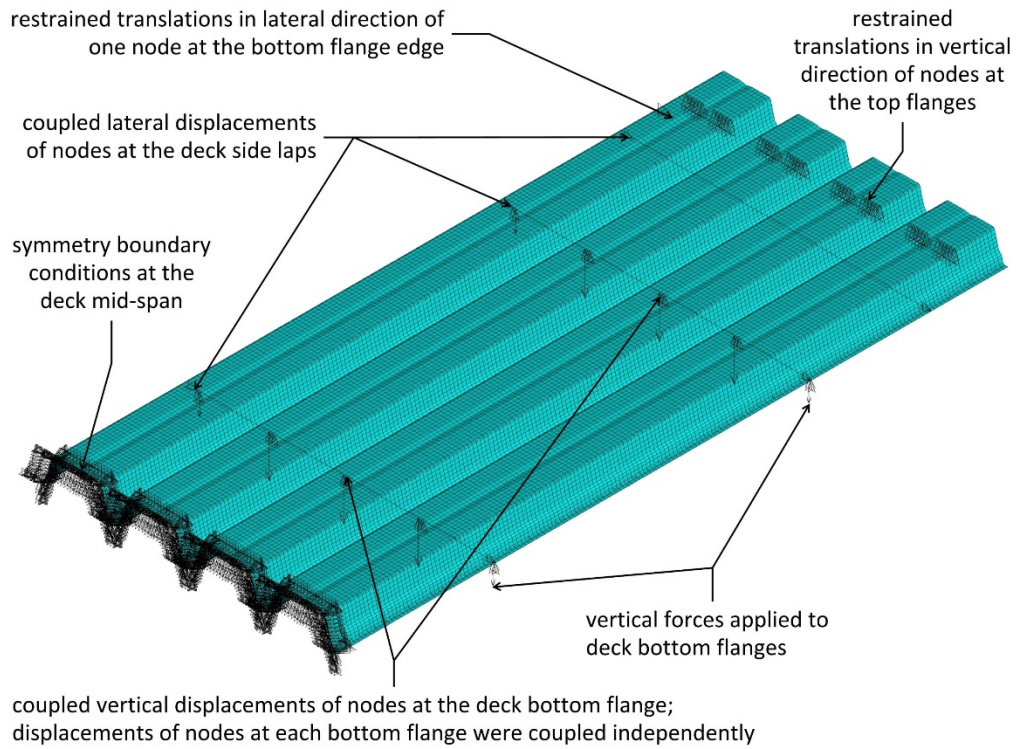


**Figure 4. Boundary conditions of deck models supported at top flanges and loaded through bottom flanges (TFS-BFL models).**

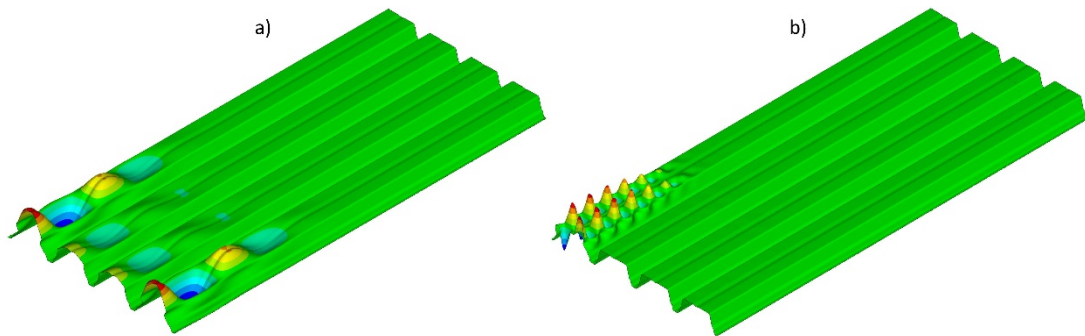


**Figure 5. Buckling modes of studied deck profiles: a) distortional elastic buckling of deck top flange; b) local elastic buckling of deck top flange.**

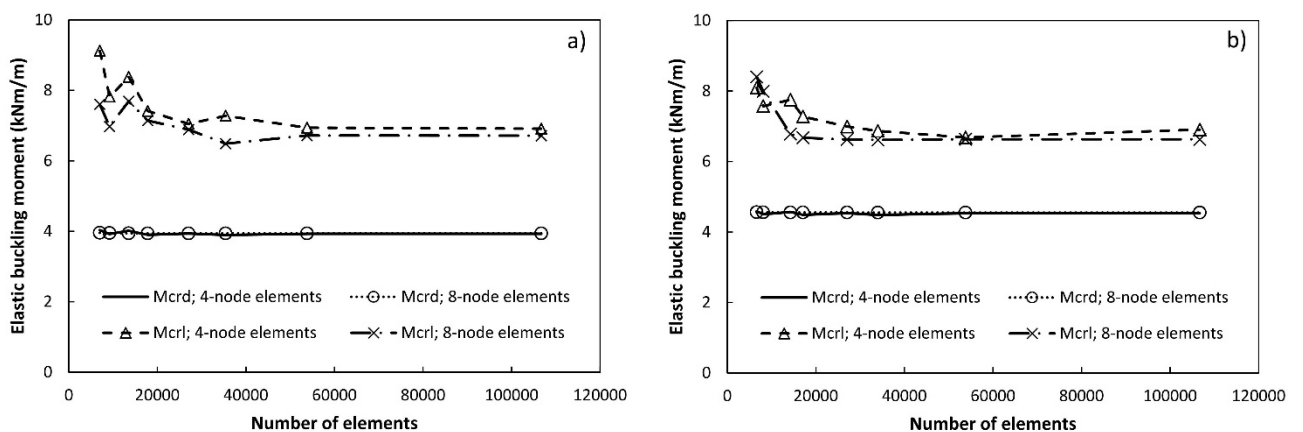


**Figure 6. Effects of FE discretization on elastic buckling moments of a) 73- and b) 56-mm deep deck.**

Figure 7 shows effects of the mesh density and the IGI magnitudes on the moment capacities of the studied profiles and average CPU time per iteration for models with different mesh densities and shell element types. The moment capacities of the 73- and 56-mm deep decks with both element types converged for the mesh densities D6 and D2, respectively. The considered IGI magnitudes had very small effects on the moment capacities. CPU time per iteration increased nearly linearly with an increase in the number of elements. The

computation time was 2–4 times (3 times on average) longer for the 8-node elements when compared with the 4-node elements.

Based on the convergence study presented herein, mesh densities D7 and D5 were selected for further studies for the deck models with the 4- and 8-node elements, respectively. The IGI magnitude of  $b_{tf}/150$  was selected for the further studies.

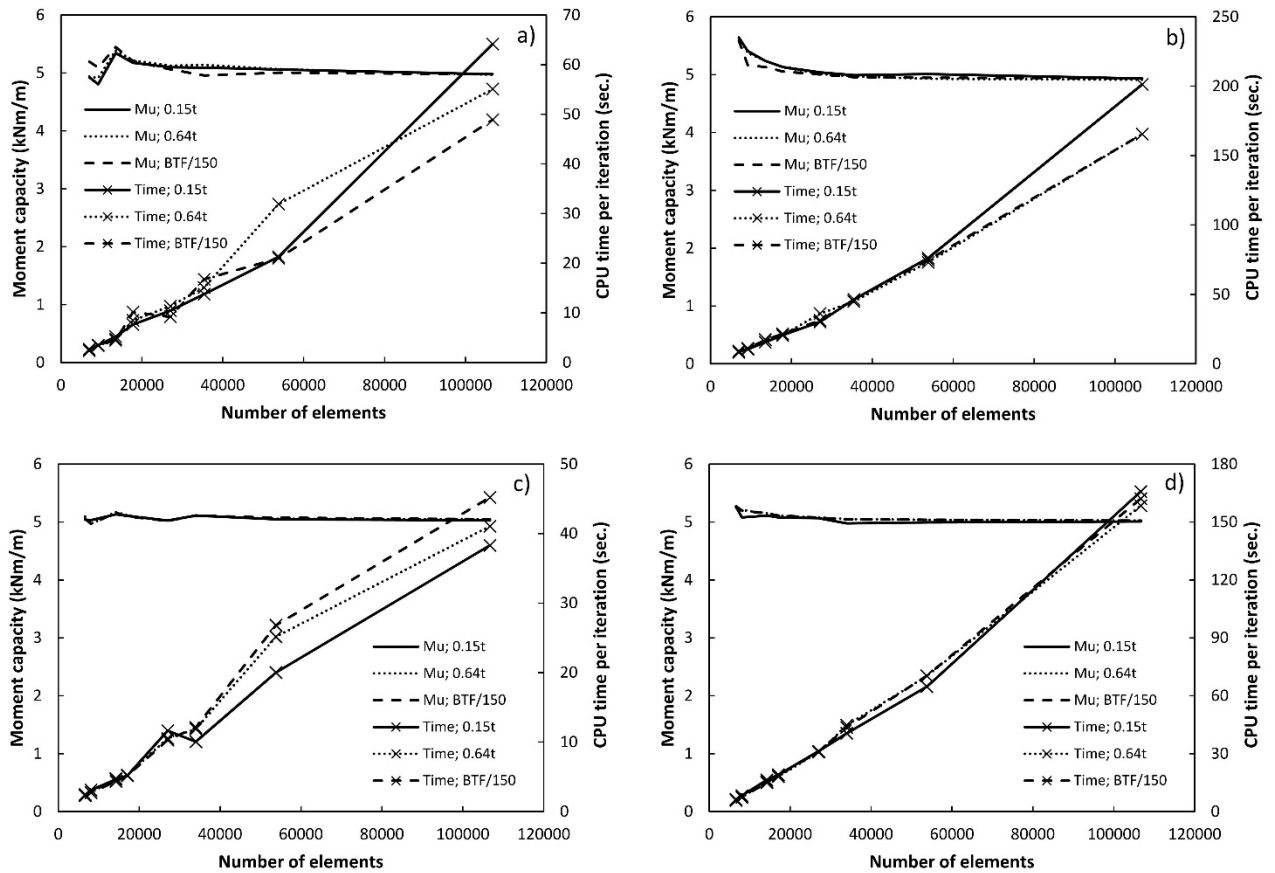


**Figure 7. Effects of FE discretization on moment capacity and computation time of a) and b) 73-mm deep deck models with 4- and 8-node elements, respectively; c) and d) 56-mm deep deck models with 4- and 8-node elements, respectively.**

### 3.2. Effects of corner radius

The effects of corner radius on the elastic buckling and ultimate moments of steel deck were studied on the profiles with the same geometry as those described in Section 3.1. Deck models with sharp corners, as well as models with the corner radii of  $6+t/2$  and  $12+t/2$  mm for the 73-mm deep deck and  $5+t/2$  and  $10+t/2$  mm for the 56-mm deep deck, were considered.

The deck was modeled with the same shell element types and material properties as those described in Section 3.1. The mesh densities D7 and D5 were used for the 4- and 8-node elements, respectively, based on the convergence study results. Boundary conditions and the analysis methods were as previously described. The IGI distributions were based on the distortional elastic buckling of the deck top flange and the IGI magnitude of  $b_{tf}/150$ .

Figure 8 shows effects of the corner radius on the elastic buckling and ultimate moments of the studied models. The corner radius in the considered ranges practically did not affect the distortional elastic buckling moment,  $M_{crd}$ , for all studied models. The local elastic buckling moments,  $M_{crl}$ , increased when the corner radius increased, which can be explained by the reduction in the flat width of the deck top flanges with the increase of the corner radius. Moment capacity,  $M_u$ , of the models reduced by 5 and 7 % for the 73- and 56-mm deck, respectively, when the corner radii increased from zero to the maximum studied values. These results show that the deck corner radius has relatively small effects on the moment capacity and the distortional elastic buckling moment. Therefore, FE deck models with sharp corners and actual corner radii can be used for studying deck strength and distortional elastic buckling moment. Deck models with sharp corners can also be used for studying the local elastic buckling moments, because they result in conservative estimates. The

corner radius should be included in FE models, however, if more accurate and realistic predictions of local elastic buckling moments are desired.

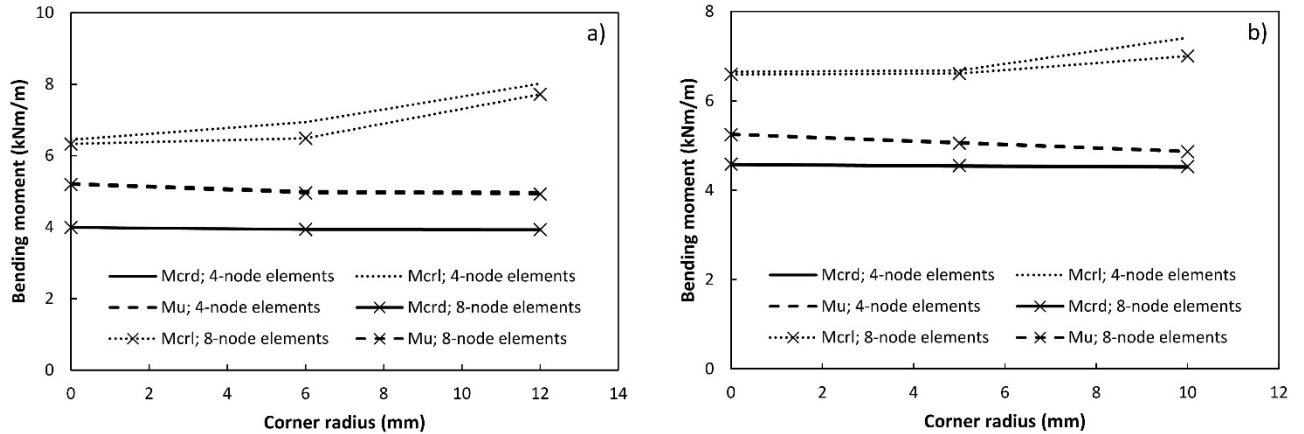


**Figure 8. Effects of corner radius on elastic buckling and ultimate moments of a) 73-mm deep deck and b) 56-mm deep deck.**

**3.3. Effects of number of deck corrugations (hats)**

A corrugated steel deck panel has a repetitive shape of the cross-section, which raises a question if modelling of only one corrugation (hat) or one-half corrugation, instead of the entire panel width, would give accurate results. To answer this question, the deck profiles analyzed in the previous stages were modeled with one-half corrugation and one corrugation. Figure 9 shows boundary conditions of the reduced-size models. To account for the panel continuity in the transverse direction, the symmetry boundary conditions were applied along the longitudinal edges of the one-half-hat and one-hat deck models. The corner radii of the models were  $6+t/2$  mm for the 73-mm deep deck and  $5+t/2$  mm for the 56-mm deep deck. All other parameters of the models were as those described in Section 3.2.

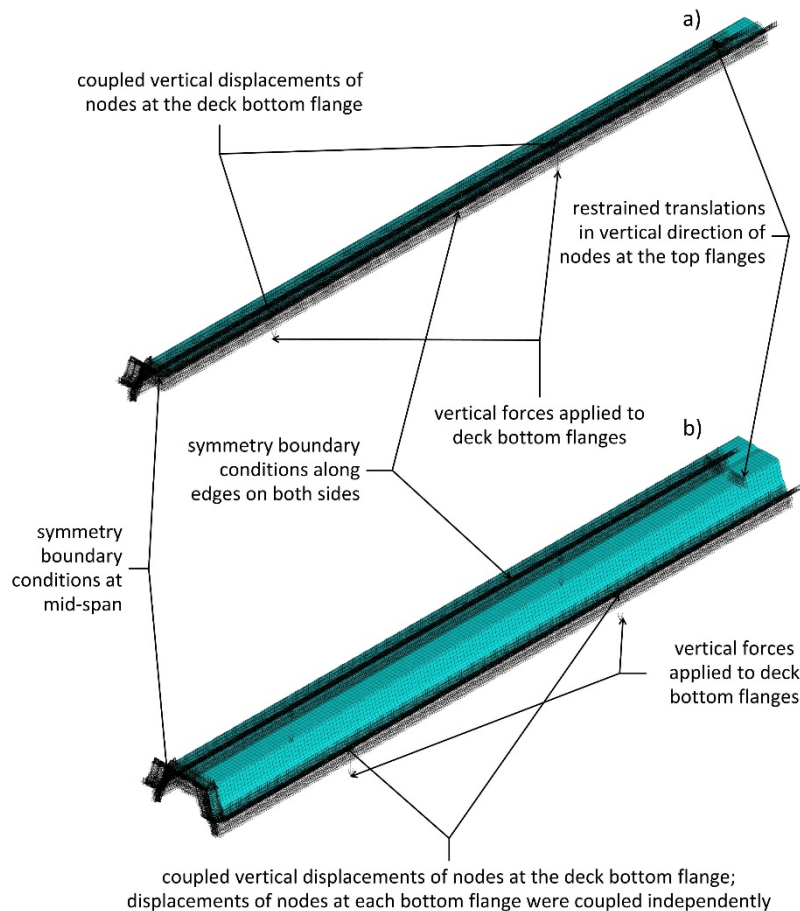


**Figure 9. Boundary conditions of reduced-size deck models: a) one-half-hat model; b) one-hat model.**

Figure 10 shows ratios of the elastic buckling and ultimate moments per unit width obtained for the one-half-hat and one-hat deck models to the moments obtained for the full-width, four-hat, models. Based on the presented results, it can be concluded that the reduced-size models provide elastic buckling moments and moment capacities identical to those predicted by the full-width models. The one-hat models were slightly more accurate than the one-half-hat models, especially in predicting the local elastic buckling load of the profile with more slender top flanges. The analyses were 6–8 times faster for the one-half-hat models and 3–5 times faster for the one-hat models when compared with the full-width models.

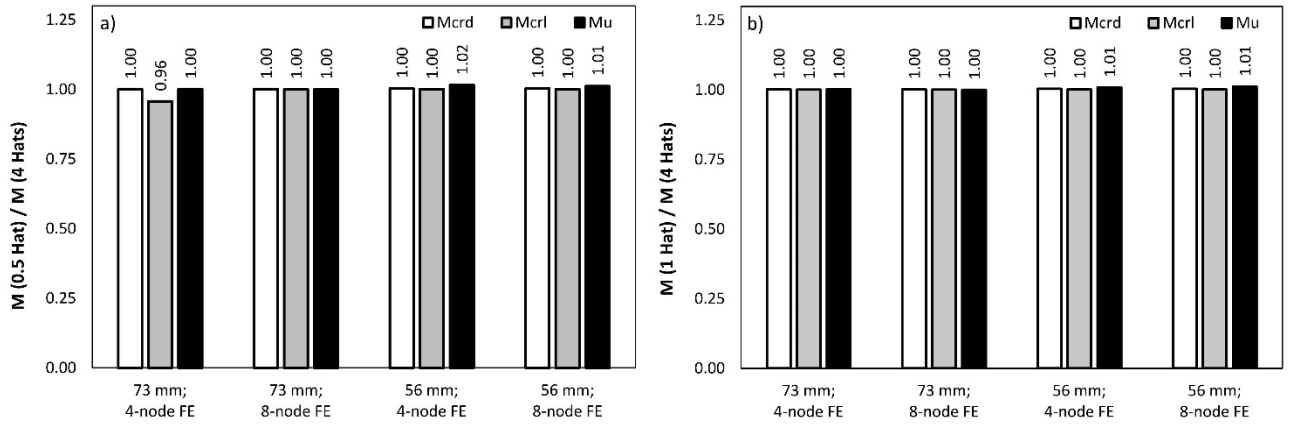


Figure 10. Ratios of elastic buckling and ultimate moments for one-half-hat models and b) one-hat models to moments for four-hat models.

### 3.4. Effects of initial geometric imperfection distribution

The first elastic buckling mode of cold-formed steel members is commonly used to model distribution of IGIs [14]. As was mentioned previously, the first elastic buckling mode of the studied profiles was distortional buckling of the deck top flanges shown in Figure 5a. The IGI distribution can also be modeled based on the local elastic buckling mode, which was one of the higher elastic buckling modes, shown in Figure 5b. To see if modeling of the IGI distribution based on the distortional and local buckling modes makes any differences in the predicted moment capacities, the full-width, four-hat, deck panels were modeled with the imperfection distributions based on the both buckling modes. The  $0.15t$ ,  $0.64t$ , and  $b_{ff}/150$  IGI magnitudes were used for both IGI distributions. All other parameters of the models were as those described in Section 3.3.

Figure 11 shows the ratios of ultimate moments for the models with the IGI distributions based on the local elastic buckling modes (LBM) to ultimate moments for the models with the IGI distributions based on the distortional elastic buckling modes (DBM). The ratios were in the ranges between 0.99 and 1.03, 0.96 and 0.99, and 0.98 and 1.00 for the IGI magnitudes of  $0.15t$ ,  $0.64t$ , and  $b_{ff}/150$ , respectively. These results show that either local or distortional elastic buckling modes can be used for modeling the IGI distributions in steel deck profiles.

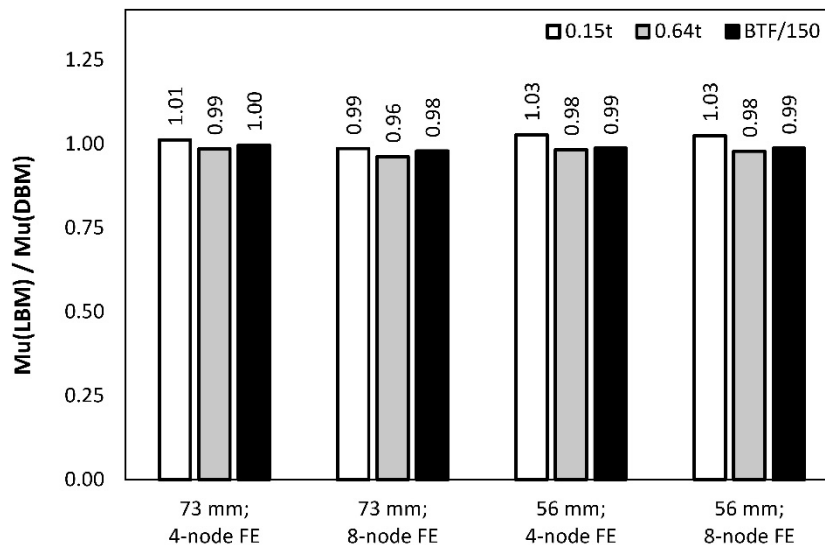
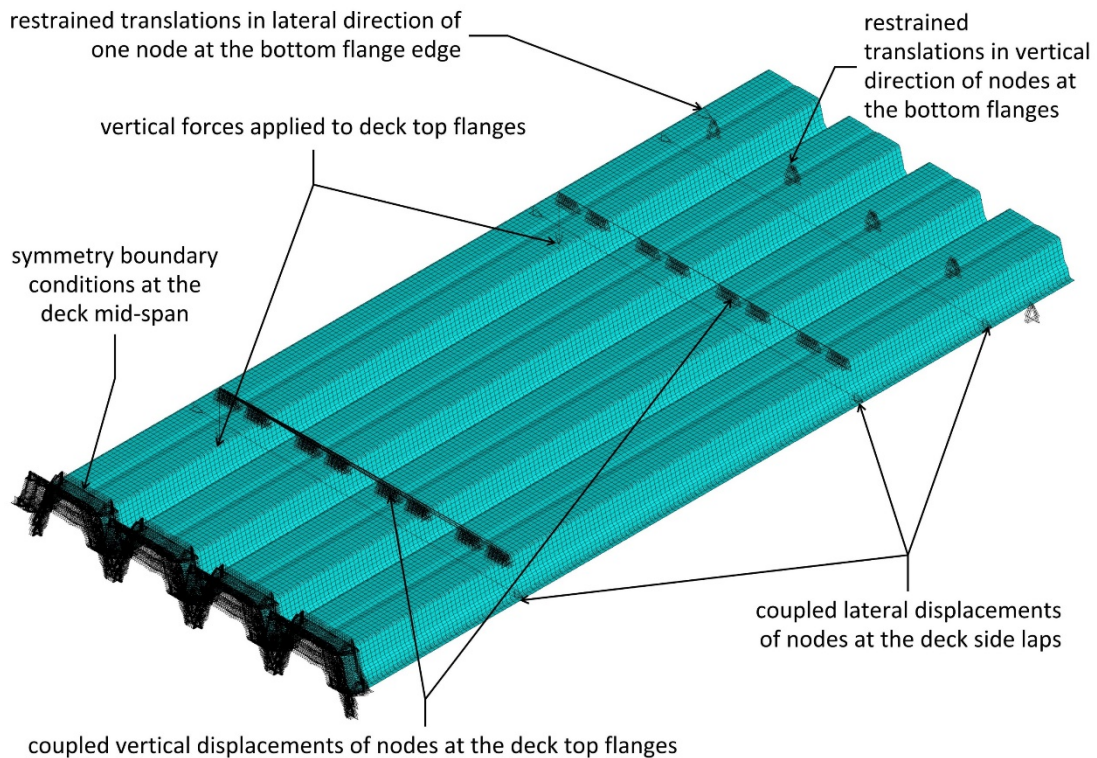


Figure 11. Ratios of ultimate moments for models with initial geometric imperfection distribution based on local elastic buckling mode to ultimate moments for models with initial geometric imperfection distribution based on distortional elastic buckling mode.

### 3.5. Effects of deck support conditions, loading application, and transverse ties

In the physical testing described in [32], the steel deck was supported at top flanges and loaded through bottom flanges to avoid the influence of local web deformations (web crippling) on the behavior and strength of the deck in bending. Transverse ties were used in the testing to prevent deck panel spreading. Steel deck can also be tested with support reactions transferred through deck bottom flanges and loads applied to deck top flanges [13]. The transverse ties may not be used in the testing.

To evaluate the effects of the boundary conditions and the transverse ties, the deck tested in [32] was modeled with the support conditions and loading application as in the tests (top-flange-supported-bottom-flange-loaded (TFS-BFL)) with and without ties, as well as with the support reactions transferred through the deck bottom flanges and loads applied to the deck top flanges (bottom-flange-supported-top-flange-loaded (BFS-TFL)) with and without ties. Figures 4 and 12 show boundary conditions for the TFS-BFL and BFS-TFL models, respectively. The IGI distributions were based on the distortional elastic buckling mode. The IGI magnitude was taken as  $b_{tfl}/150$ . All other model parameters were as those described in Section 3.4.



**Figure 12. Boundary conditions of deck models supported at bottom flanges and loaded through top flanges (BFS-TFL models).**

Figure 13 shows the effects of the studied boundary conditions on the elastic buckling and ultimate moments. Figures 13a and 13b show the ratios of moments for the BFS-TFL models to the moments for the TFS-BFL models without and with ties, respectively. When no transverse ties were provided, the distortional elastic buckling moments,  $M_{crd}$ , for the BFS-TFL models were 2–6 % greater than those for the TFS-BFL models. The local elastic buckling moments,  $M_{crl}$ , and ultimate moments,  $M_u$ , for the BFS-TFL models were 0–10 % and 3–7 %, respectively, smaller than those for the TFS-BFL models. When transverse ties were provided, the  $M_{crd}$ ,  $M_{crl}$ , and  $M_u$  values for the BFS-TFL models were 1 % smaller or 1–5 % greater, 1–6 % smaller or 1–4 % greater, and 1 % smaller or 0–1 % greater, respectively, than those for the TFS-BFL models. These results show that the moment capacity of steel deck models without transverse ties is more sensitive to the change in the boundary conditions than the moment capacity of steel deck models with transverse ties. In the presence of the transverse ties, the differences in the moment capacities of the deck with the different boundary conditions considered in this study were very small. The elastic buckling moments of deck models with ties were also less sensitive to the change in the boundary conditions when compared with the models without ties.

Figure 13c shows the ratios of moments for the TFS-BFL models without ties to moments for the TFS-BFL models with ties. The  $M_{crd}$  values reduced by 3–4 %, while the  $M_{crl}$  values either reduced by 2–4 % or increased by 3 %, when the transverse ties were removed from the TFS-BFL models. The transverse ties removal resulted in an increase of the  $M_u$  values by 1 % for the 73-mm deep by 0.75-mm thick profile, whereas the 56-mm deep by 1.00-mm thick profile demonstrated a 7 % reduction in the moment capacities.

Figure 13d shows ratios of moments for the BFS-TFL models without ties to moments for the BFS-TFL models with ties. For the BFS-TFL models, the  $M_{crd}$ ,  $M_{crl}$ , and  $M_u$  values reduced by 2, 0–6, and 5–10 %, respectively, when the transverse ties were eliminated.

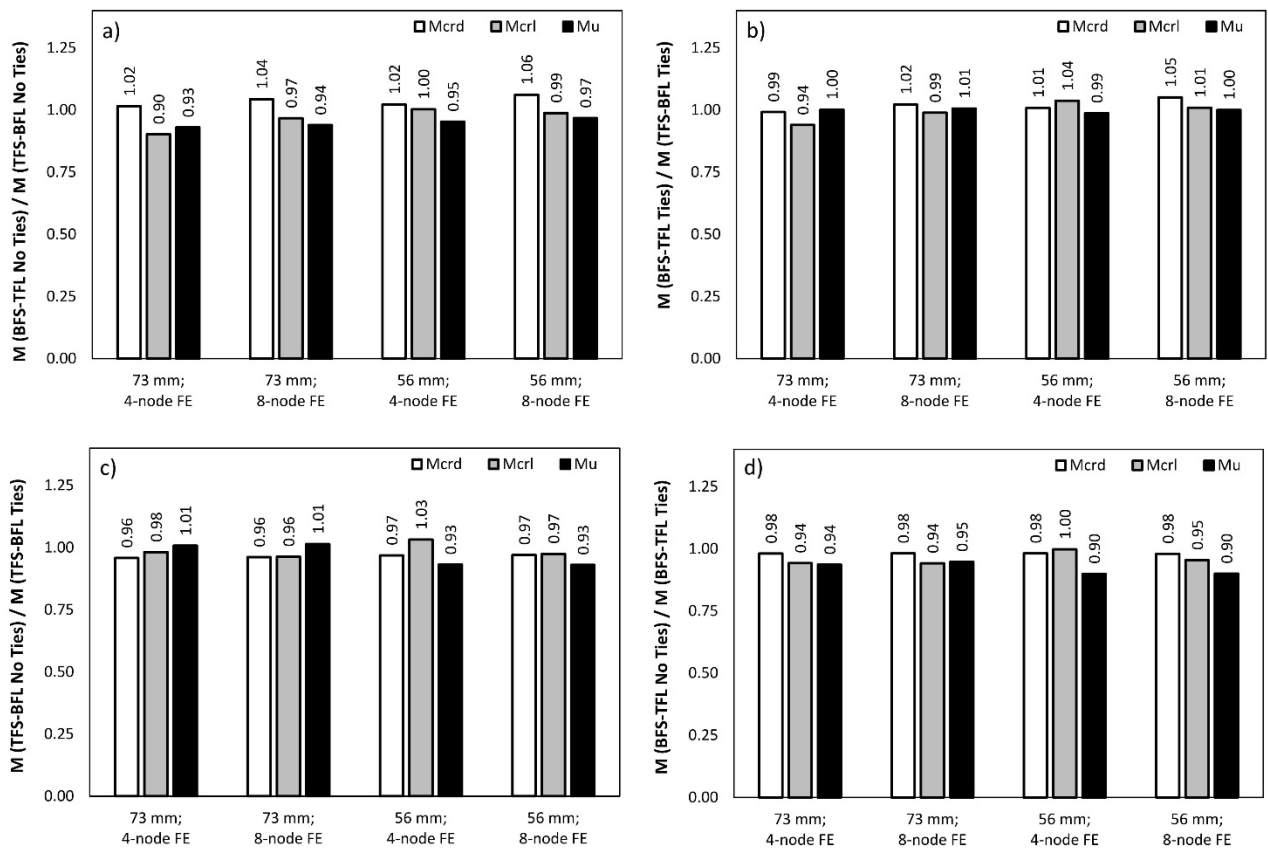


**Figure 13. Ratios of elastic buckling and ultimate moments for a) and b) BFS-TFL models to moments for TFS-BFL models without ties and with ties, respectively; c) TFS-BFL models without ties to moments for TFS-BFL models with ties; d) BFS-TFL models without ties to moments for BFS-TFL models with ties.**

These results show that addition of the transverse ties generally increases the elastic buckling and ultimate moments of steel deck profiles. The BFS-TFL models are more sensitive to the transverse ties than the TFS-BFL models. The beneficial effects of transverse ties were more pronounced for the thicker deck profiles.

### 3.6. Effects of loading type

In the physical testing [32], four concentrated loads evenly spaced along the span were applied to the deck. Structural members are also often tested in four-point bending. This loading diagram may be more convenient for FE modeling, because it allows to load the member by imposed displacements, which makes possible obtaining full load-displacement curves with descending branches. In the real life, steel deck is designed for uniformly distributed loads. To study the effects of the different loading types on the elastic buckling and ultimate moments, FE models of the deck with the following additional loading types were analyzed:

- 1) two equal line loads applied as forces along lines parallel to deck supports and located at the distance of  $L/3$  (where  $L$  is deck span length) from each deck support,
- 2) two equal displacements applied along lines parallel to deck supports and located at the distance of  $L/3$  from each deck support, and
- 3) a uniformly distributed load.

Boundary conditions of the models with the different loading types were similar to those shown in Figure 4, except the loads were applied as forces or displacements at the third points or as a uniformly distributed load. The material properties of the deck and corner radii were as those described in Section 3.1. The IGI distribution was based on the distortional elastic buckling of the deck top flanges with the IGI magnitude of  $b_{tf}/150$ .

Figures 14a, 14b, and 14c show ratios of the elastic buckling and ultimate moments obtained for the models loaded by two line forces, two displacements, and a uniform load, respectively, to those obtained for the models loaded by four line forces. The presented comparisons indicate that all studied loading types resulted in comparable predictions of the elastic buckling and ultimate moments. The differences in the

predictions of the  $M_{crd}$ ,  $M_{crl}$ , and  $M_u$  values were within 1, 5, and 5 %, respectively. These results demonstrate that any of the studied loading types can be used for numerical studies of elastic buckling and ultimate moments of corrugated steel deck profiles.

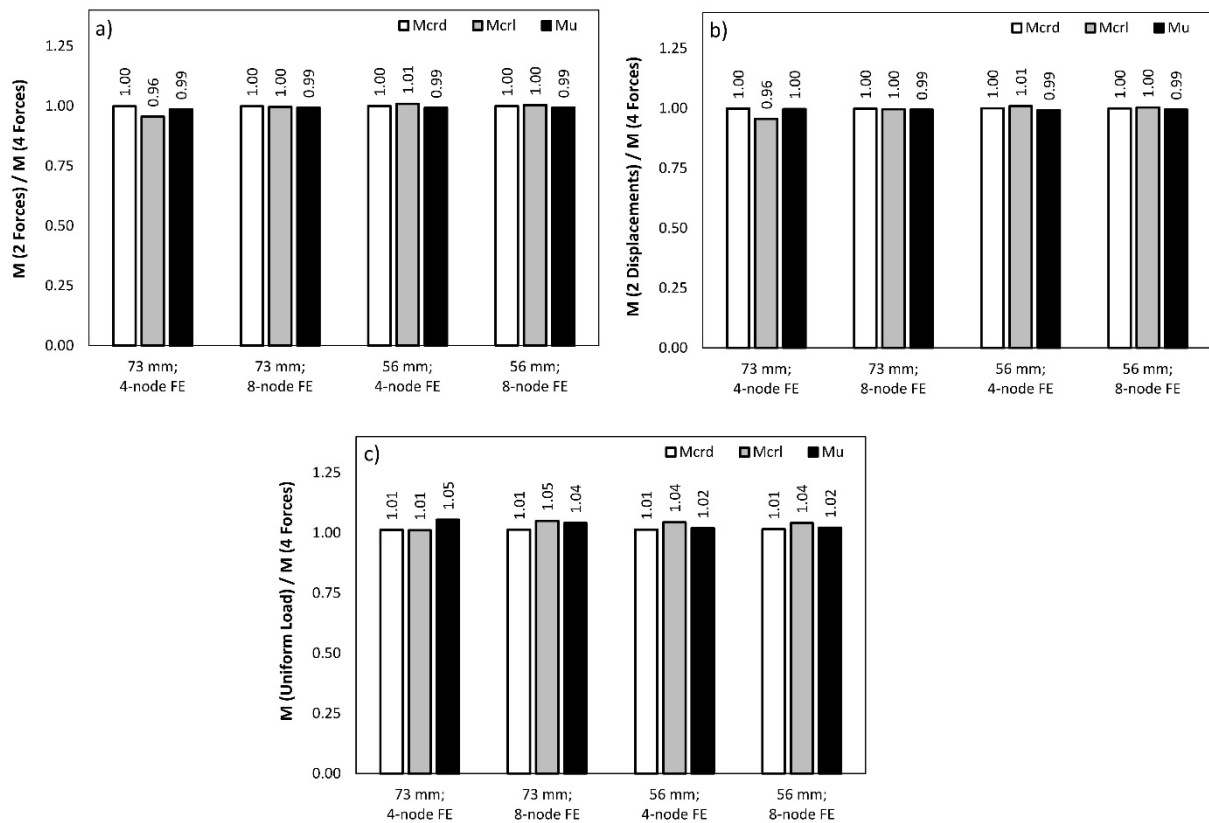


**Figure 14. Ratios of elastic buckling and ultimate moments for a) models loaded by two forces, b) models loaded by two displacements, and c) models loaded by uniform load to moments for models loaded by four forces.**

### 3.7. Effects of steel stress-strain diagrams and model validation

All deck models described previously were based on the nonlinear stress-strain curves proposed in [34]. Simplified models, such as elastic-perfectly plastic and bilinear, are also commonly used for modeling the behavior and strength of steel members. To study the effects of different stress-strain diagrams on the structural response, flexural stiffness, and moment capacity of the deck, all solid deck profiles tested in [32] were modeled with the elastic-perfectly plastic, bilinear, and nonlinear stress-strain diagrams shown in Figure 2. The key parameters of the diagrams, such as steel yield stress,  $f_y$ , and tensile strength,  $f_u$ , were as those reported in [32].

The FE simulation results obtained in this stage were also compared with the experimental data to validate the developed FE models. Overall, 14 physical test results described in [32] were used for the model validation. In addition to the 73-mm deep by 0.75-mm thick and 56-mm deep by 1.00-mm thick profiles described previously, 73-mm deep by 1.00-mm thick and 56-mm deep by 0.75-mm thick profiles were modeled and analyzed. Mesh densities D7 and D5 (see Table 1) were used for deck models with the 4- and 8-node elements, respectively. Corner radii and boundary conditions were as those described in Section 3.1. The IGI distribution was based on the distortional elastic buckling of the deck top flange with the IGI magnitude of  $b_{fd}/150$ .

Figure 15 shows load-deflection diagrams obtained from the tests [32] and the FE simulations of deck models with different steel stress-strain diagrams and element types. The EPP, BL, and NL abbreviations in Figure 15 stand for elastic-perfectly plastic, bilinear, and nonlinear stress-strain diagrams of steel. Deliveries 1 and 3 shown in Figure 15 refer to deck made from different coils of steel and delivered to the testing lab at different times [32]. The structural response of the 4-node element models with mesh density D7 and the 8-node element models with mesh density D5 were nearly identical. The models based on the elastic-perfectly plastic and bilinear constitutive models did not show noticeable differences in the structural response either. The nonlinear stress-strain diagram resulted in considerably different structural response of the models when compared with the elastic-perfectly plastic and bilinear diagrams due to the plastic deformation of steel at stresses below the yield stress accounted for by the nonlinear model. Figure 15 shows that the nonlinear

stress-strain diagram generally resulted in a better agreement of flexural stiffness of the deck models with the test results for the full range of loading.

Figure 16 compares the ultimate moments of deck models with different constitutive models and element types obtained from the FE simulations with the test results [32]. It can be concluded that the developed FE models with all studied stress-strain diagrams and element types showed good agreements with the experimental data. The nonlinear stress-strain diagrams, however, resulted in slightly better predictions of the ultimate moments when compared with the elastic-perfectly plastic and bilinear diagrams for both the 4- and 8-node shell elements.

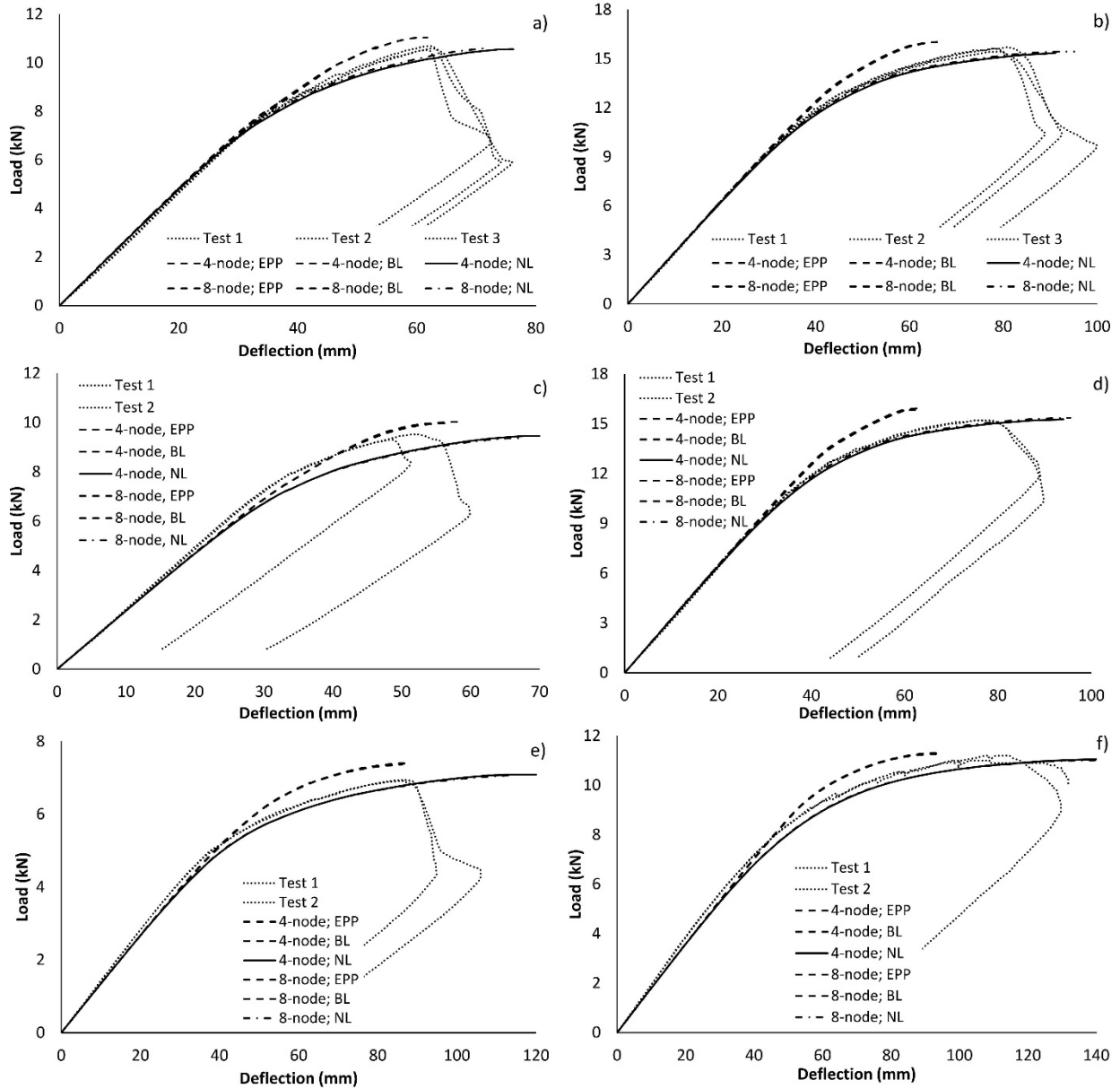


**Figure 15. Load-deflection diagrams from tests and FE simulations: a) and c) 73-mm by 0.75-mm deck from delivery 3 and 1, respectively; b) and d) 75-mm by 1.00-mm deck from delivery 3 and 1, respectively; e) and f) 56-mm by 0.75-mm and 1.00-mm, respectively.**

Figure 17 compares deck deflections at the maximum moments from the FE simulations and the tests [32]. The FE models with the elastic-perfectly plastic and bilinear stress-strain diagrams slightly underestimated the deck deflections at the maximum moments, whereas the FE models with the nonlinear stress-strain diagram overestimated the maximum deck deflections. The nonlinear diagrams resulted in a smaller scatter of the FEA/Test ratios when compared with the elastic-perfectly plastic and bilinear stress-strain diagrams. The nonlinear stress-strain diagrams of the steel might be adjusted if needed, by reducing the  $\epsilon_u$  value, to improve predictions of the deck deflection at the maximum moment. This characteristic, however, is not very important for the practical design of steel decks.

A more important characteristic of the deck flexural stiffness is the deck deflection at the service level load, which is compared with the acceptable deck deflection in the structural deck design. The service level

load is commonly assumed to be at 60 % of the ultimate moment. Figure 18 shows comparisons of deck deflections at  $0.6M_u$  obtained from the FE simulations with the test results. The FE models with the material behavior of steel described by the nonlinear stress-strain diagram show a better agreement of deflections at the service level loads with the test results when compared with the models based on the simplified stress-strain diagrams. The latter, however, also show reasonably good agreements with the test results.

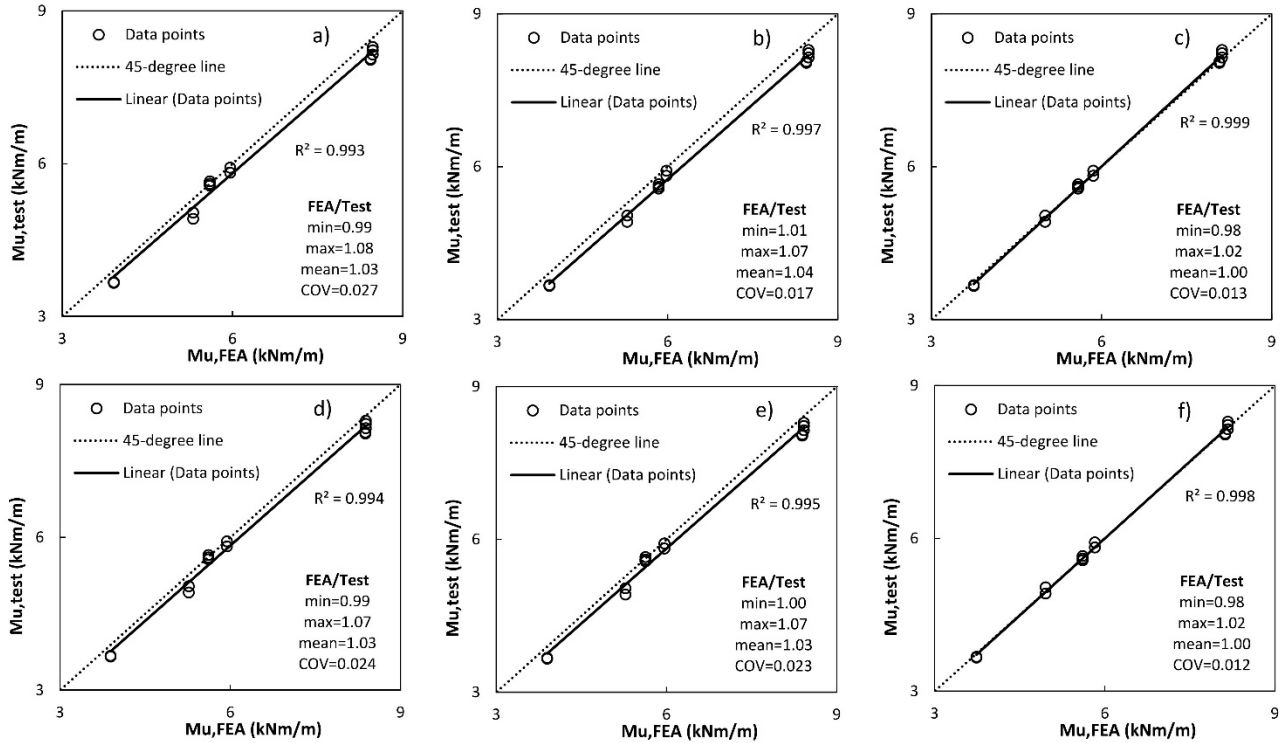


**Figure 16. Comparisons of ultimate moments for deck models with different constitutive models and element types from FE simulations with test results: a), b), and c) 4-node FE models with elastic-perfectly plastic, bilinear, and nonlinear stress-strain diagrams, respectively; d), e), and f) 8-node FE models with elastic-perfectly plastic, bilinear, and nonlinear stress-strain diagrams, respectively.**

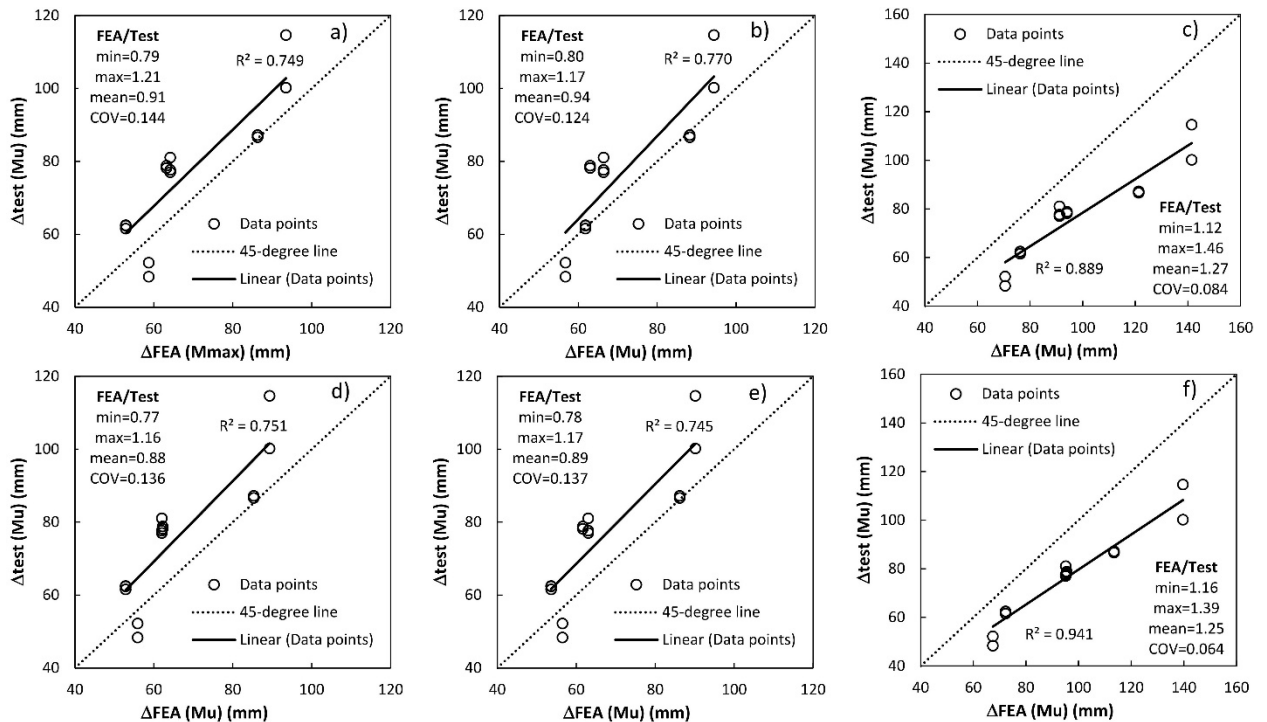


**Figure 17. Comparisons of deck deflections at ultimate moments for models with different constitutive models and element types obtained from FE simulations with test results: a), b), and c) 4-node FE models with elastic-perfectly plastic, bilinear, and nonlinear stress-strain diagrams, respectively; d), e), and f) 8-node FE models with elastic-perfectly plastic, bilinear, and nonlinear stress-strain diagrams, respectively.**

It can be concluded that the nonlinear stress-strain diagrams used in the FE simulations result in better agreements of strength and flexural stiffness of steel deck with the experimental data than the simplified elastic-perfectly plastic and bilinear models. The developed models can be employed for numerical studies of solid deck profiles and can be used as a basis for the development of FE models of steel deck with openings and acoustical perforations, as well as built-up deck profiles.

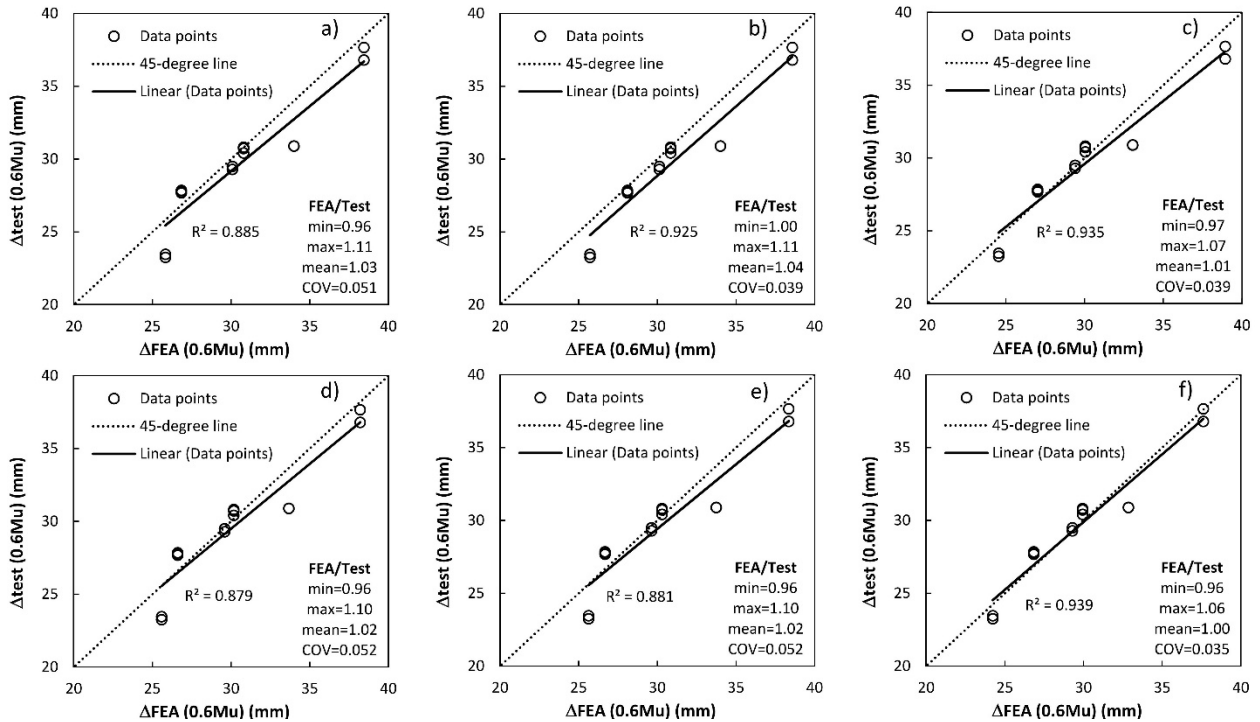


**Figure 18. Comparisons of deck deflections at service level moments for models with different constitutive models and element types obtained from FE simulations with test results: a), b), and c) 4-node FE models with elastic-perfectly plastic, bilinear, and nonlinear stress-strain diagrams, respectively; d), e), and f) 8-node FE models with elastic-perfectly plastic, bilinear, and nonlinear stress-strain diagrams, respectively.**

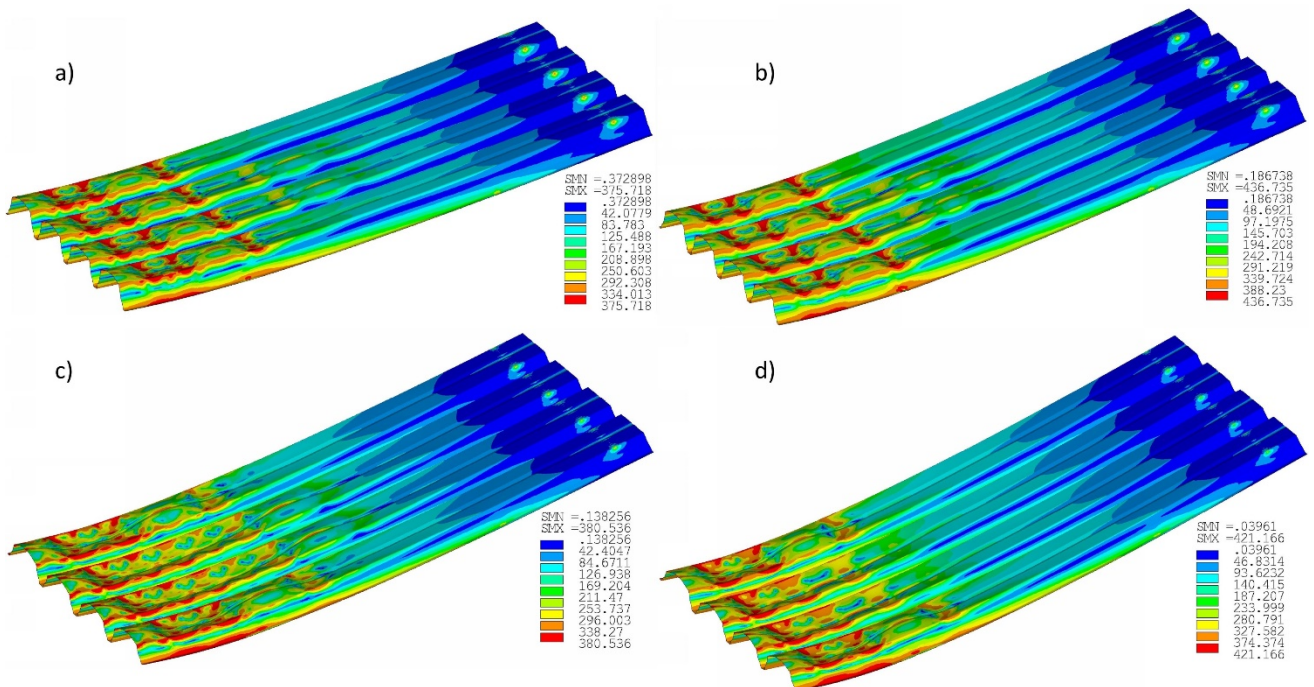


**Figure 19. von Mises stresses [MPa] in FE deck models at ultimate moments: a) and b) 73-mm by 0.75- and 1.00-mm deck, respectively; c) and d) 56-mm by 0.75- and 1.00-mm deck, respectively.**

Figure 19 shows von Mises stresses in the FE deck models at the ultimate moments. Nonlinear distortional buckling of the deck top flanges can be clearly seen for all studied deck heights and steel thicknesses. This type of buckling was observed in the tests [32] as well. Highly non-uniform von Mises stress distributions along and across the deck top flanges due to the flange nonlinear buckling can be seen in Figure 19. Higher von Mises stresses were observed near the corners and within unbuckled portions of the flanges.

## 4. Conclusions

1. FE models of corrugated cold-formed steel deck were developed in a commercially available FE simulation software, ANSYS. Steel deck was modeled with linear 4-node and quadratic 8-node structural shell elements. Optimal mesh densities were determined for the deck models with both element types based on a convergence study. The effects of different constitutive steel models on the moment capacity, flexural stiffness, and load-deflection diagrams were considered.

2. The study showed that the deck corner radius had relatively small effects on the moment capacity and the distortional elastic buckling moment, but had a greater effect on the local elastic buckling moment.

3. Reduced-size FE deck models, with only one hat or one-half hat instead of the full-width deck panel with multiple hats, were studied. The reduced-size FE models provided elastic buckling and ultimate moments identical to those predicted by the full-size models.

4. IGI distributions based on the distortional and local elastic buckling modes of the deck top flange with three different IGI magnitudes were studied. The studied IGI distributions and magnitudes had relatively small effects on moment capacities of the FE deck models.

5. Effects of different boundary conditions (with the deck supported at top flanges and loaded through bottom flanges; and with the deck supported at bottom flanges and loaded through top flanges) and transverse ties were studied. The elastic buckling and ultimate moments of the models without transverse ties were more sensitive to the change in the boundary conditions when compared with the models with transverse ties. Addition of the transverse ties resulted in increases in the elastic buckling and ultimate moments, especially for thicker profiles. Deck models supported at bottom flanges and loaded through top flanges were more sensitive to the presence of the transverse ties than the models supported at top flanges and loaded through bottom flanges.

6. Effects of different loading types along the deck span, such as four loads modeled as forces, two loads modeled as forces and imposed displacements, and a uniform load, were considered. The elastic buckling and ultimate moments obtained for the studied loading types showed very small differences.

7. The developed models were validated against available test results. Moment capacities, flexural stiffness values, and load-deflection curves predicted by the models compared well with those obtained from physical testing, especially when nonlinear stress-strain diagrams of steel were used.

8. The developed FE models can be an efficient tool for numerical studies of flexural strength and stiffness of non-perforated steel deck with various geometry under various loading types, which can be useful in development of new efficient profiles and in improving current deck design methods. They may also form a basis for development of FE models of deck with openings and perforations, as well as built-up deck profiles, design methods for which are currently underdeveloped.

## References

1. ANSI/SDI RD-2017. Standard for steel roof deck. Steel Deck Institute; 2017.
2. AISI S100-16. North American specification for the design of cold-formed steel structural members. American Iron and Steel Institute. Washington, DC; 2016.
3. AS/NZS 4600:2018. Cold-formed steel structures. Standards Australia/Standards New Zealand. Sidney, Australia; 2018.
4. EN 1993-1-3:2006. Eurocode 3 – Design of steel structures – Part 1–3: General rules – Supplementary rules for cold-formed members and sheeting. European Committee for Standardization. Brussels, Belgium; 2006.
5. SDI MOC3. Manual of construction with steel deck. 3rd ed. Steel Deck Institute; 2016.
6. SDI RDDM1. Roof deck design manual. 1st ed. Steel Deck Institute; 2012.
7. Palisson, A. Guidelines and recommendations for integrating specific profiled steels sheets in Eurocodes (GRISPE). [Online]. D 3.1 Perforated Profiles. Sokol Palisson Consultants. Paris, France, 2018. URL: <http://www.grispeplus.eu/7-families-of-steel-profiles/perforated-and-holed-profiles/>
8. Degtyarev, V.V., Degtyareva, N.V. Elastic stability of uniformly compressed plates perforated in triangular patterns. *Thin-Walled Structures*. 2012. 52. Pp. 165–173.
9. Palisson, A. Guidelines and recommendations for integrating specific profiled steels sheets in Eurocodes (GRISPE). D 3.1 Holed Profiles. Sokol Palisson Consultants. Paris, France, 2018. <http://www.grispeplus.eu/7-families-of-steel-profiles/perforated-and-holed-profiles/>
10. Degtyarev, V.V. A finite element study of corrugated steel deck subjected to concentrated loads. *Proceedings of Wei-Wen Yu International Specialty Conference on Cold-Formed Steel Structures 2018*. St. Louis, Missouri, USA, 2018. Pp. 731–745.
11. Degtyarev, V.V. Concentrated load distribution in corrugated steel decks: A parametric finite element study. *Engineering Structures*. 2020. 206. 110158.
12. Dudenbostel, R.K., Sputo, T. Application of the Direct Strength Method to steel deck. *Proceedings of Wei-Wen Yu International Specialty Conference on Cold-Formed Steel Structures 2016*. Baltimore, Maryland, USA, 2016. Pp. 665–679.
13. Raebel, C., Gwozdz, D. Comparison of experimental and numerical results for flexural capacity of light-gage steel roof deck. *Proceedings of Wei-Wen Yu International Specialty Conference on Cold-Formed Steel Structures 2018*. St. Louis, Missouri, USA, 2018. Pp. 55–67.
14. Schafer, B.W., Li, Z., Moen, C.D. Computational modeling of cold-formed steel. *Thin-Walled Structures*. 2010. 48. Pp. 752–762.

15. Yu, C., Schafer, B.W. Simulations of cold-formed steel beams in local and distortional buckling with applications to the direct strength method. *Journal of Constructional Steel Research*. 2007. 63. Pp. 581–590.
16. Haidarali, M.R., Nethercot, D.A. Finite element modelling of cold-formed steel beams under local buckling or combined local/distortional buckling. *Thin-Walled Structures*. 2011. 49. Pp. 1554–1562.
17. Nazmeeva, T.V., Vatin, N.I. Numerical investigations of notched C-profile compressed members with initial imperfections. *Magazine of Civil Engineering*. 2016. 62(2). Pp. 92–101.
18. Garifullin, M., Nackenhorst, U. Computational analysis of cold-formed steel columns with initial imperfections. *Procedia Engineering*. 2015. 117. Pp. 1073–1079.
19. Salhab, B., Wang, Y.C. Equivalent thickness of cold-formed thin-walled channel sections with perforated webs under compression. *Thin-Walled Structures*. 2008. 46. Pp. 823–838.
20. Pham, C.H., Hancock, G.J. Numerical simulation of high strength cold-formed purlins in combined bending and shear. *Journal of Constructional Steel Research*. 2010. 66(10). Pp. 1205–1217.
21. Pham, C.H., Hancock, G.J. Numerical investigation of longitudinally stiffened web channels predominantly in shear. *Thin-Walled Structures*. 2015. 86. Pp. 47–55.
22. Hui, C., Gardner, L., Nethercot, D.A. Moment redistribution in cold-formed steel continuous beams. *Thin-Walled Structures*. 2016. 98. Pp. 465–477.
23. Keerthan, P., Mahendran, M. Numerical modeling of Lite Steel beams subject to shear. *Journal of Structural Engineering*. 2011. 137(12). Pp. 1428–1439.
24. Keerthan, P., Mahendran, M., Hughes, D. Numerical studies and design of hollow flange channel beams subject to combined bending and shear actions. *Engineering Structures*. 2014. 75. Pp. 197–212.
25. Sundararajah, L., Mahendran, M., Keerthan, P. Numerical Modeling and Design of Lipped Channel Beams Subject to Web Crippling under One-Flange Load Cases. *Journal of Structural Engineering*. 2019. 145(10). Pp. 1–16.
26. Degtyarev, V.V., Degtyareva, N.V. Numerical simulations on cold-formed steel channels with flat slotted webs in shear. Part I: Elastic shear buckling characteristics. *Thin-Walled Structures*. 2017. 119. Pp. 22–32.
27. Degtyarev, V.V., Degtyareva, N.V. Numerical simulations on cold-formed steel channels with flat slotted webs in shear. Part II: Ultimate shear strength. *Thin-Walled Structures*. 2017. 119. Pp. 211–223.
28. Degtyarev, V.V., Degtyareva, N.V. Numerical simulations on cold-formed steel channels with longitudinally stiffened slotted webs in shear. *Thin-Walled Structures*. 2018. 129. Pp. 429–456.
29. Degtyareva, N., Gatheeshgar, P., Poologanathan, K., Gunalan, S., Lawson, M., Sunday, P. Combined bending and shear behaviour of slotted perforated steel channels: Numerical studies. *Journal of Constructional Steel Research*. 2019. 161. Pp. 369–384.
30. Misiek, Th. Tragverhalten dünnwandiger Bauteile aus perforierten Blechen (Load-bearing behaviour of thin-walled building components made of perforated sheets). Dr-Ing. Dissertation. Universität Fridericiana zu Karlsruhe. Karlsruhe, Germany. 2008. 259 p.
31. ANSYS Mechanical APDL, Release 19.2.
32. Fauth, C. Guidelines and recommendations for integrating specific profiled steels sheets in Eurocodes (GRISPE) [Online]. D 3.3 Test report. Karlsruhe Institute of Technology (KIT). Karlsruhe, Germany, 2015 (Rev.4). URL: <http://www.grispeplus.eu/7-families-of-steel-profiles/perforated-and-holed-profiles/>
33. EN 10346:2009. Continuously hot-dip coated steel flat products – Technical delivery conditions. European Committee for Standardization. Brussels, Belgium; 2009.
34. Gardner, L., Yun, X. Description of stress-strain curves for cold-formed steels. *Construction and Building Materials*. 2018. 189. Pp. 527–538.
35. EN 1993-1-5:2006. Eurocode 3 – Design of steel structures – Part 1–5: Plated structural elements. European Committee for Standardization. Brussels, Belgium; 2006.
36. Camotim, D., Silvestre, N. GBT-based analysis of the distortional postbuckling behavior of cold-formed steel z-section columns and beams. *Proceedings of the 4th International Conference on Thin-Walled Structures*. Loughborough, 2004. Pp. 243–250.
37. Schafer, B.W., Peköz, T. Computational modeling of cold-formed steel: characterizing geometric imperfections and residual stresses. *Journal of Constructional Steel Research*. 1998. 47. Pp. 193–210.

## Contacts:

*Vitaliy Degtyarev, vitaliy.degtyarev@newmill.com*

© Degtyarev, V.V., 2020